RESEARCH ARTICLE

National Science Review
9: nwab098, 2022
https://doi.org/10.1093/nsr/nwab098
Advance access publication 31 May 2021

MATERIALS SCIENCE

Special Topic: Two-dimensional Functional Materials

High-performance polarization-sensitive photodetectors on two-dimensional β-InSe

Zhinan Guo[1,†], Rui Cao[1,†], Huide Wang[1,†], Xi Zhang[2,†], Fanxu Meng[1], Xue Chen[5], Siyan Gao[2], David K. Sang[1], Thi Huong Nguyen[3], Anh Tuan Duong[3], Jinlai Zhao[1], Yu-Jia Zeng[1], Sunglae Cho[3], Bing Zhao[4], Ping-Heng Tan[5], Han Zhang[1,*] and Dianyuan Fan[1]

[1]Institute of Microscale Optoelectronics, International Collaborative Laboratory of 2D Materials for Optoelectronics Science and Technology, College of Physics and Optoelectronic Engineering, Shenzhen University, Shenzhen 518060, China; [2]Institute of Nanosurface Science and Engineering, Guangdong Provincial Key Laboratory of Micro/Nano Optomechatronics Engineering, Shenzhen University, Shenzhen 518060, China; [3]Department of Physics and Energy Harvest-Storage Research Center, University of Ulsan, Ulsan 680-749, South Korea; [4]State Key Laboratory of Supramolecular Structure and Materials, Jilin University, Changchun 130012, China and [5]State Key Laboratory of Superlattices and Microstructures, Institute of Semiconductors, Chinese Academy of Sciences, Beijing 100083, China

*Corresponding author. E-mail: hzhang@szu.edu.cn
†Equally contributed to this work.

Received 9 January 2021; **Revised** 19 May 2021; **Accepted** 24 May 2021

ABSTRACT

Two-dimensional (2D) indium selenide (InSe) has been widely studied for application in transistors and photodetectors, which benefit from its excellent optoelectronic properties. Among the three specific polytypes (γ-, ε- and β-phase) of InSe, only the crystal lattice of InSe in β-phase (β-InSe) belongs to a non-symmetry point group of D_{6h}^{4}, which indicates stronger anisotropic transport behavior and potential in the polarized photodetection of β-InSe-based optoelectronic devices. Therefore, we prepare the stable p-type 2D-layered β-InSe via temperature gradient method. The anisotropic Raman, transport and photoresponse properties of β-InSe have been experimentally and theoretically proven, showing that the β-InSe-based device has a ratio of 3.76 for the maximum to minimum dark current at two orthogonal orientations and a high photocurrent anisotropic ratio of 0.70 at 1 V bias voltage, respectively. The appealing anisotropic properties demonstrated in this work clearly identify β-InSe as a competitive candidate for filter-free polarization-sensitive photodetectors.

Keywords: 2D materials, polarization, photodetectors, β-InSe, Raman spectra

INTRODUCTION

With regard to extracting the polarization information of incident light, polarization-sensitive photodetectors (PSPDs) exhibit significant practical application in both military and civil areas, like bio-imaging [1], remote sensing [2], night vision [3] and helmet-mounted sight for fighter planes [4]. Optical filters combined with polarizers are usually needed for traditional photodetectors to realize polarized light detection. But this increases the size and complexity of devices [5]. To obtain a small-sized PSPD, one-dimensional (1D) nanomaterials with geometrical anisotropy, such as nanowires, nanoribbons and nanotubes [6,7], have been used as sensitive materials for PSPDs, which can directly identify the polarization information of incident light without any optical filters and polarizers. However, it is not an easy task to pattern and integrate these 1D nanochannels for mass production of PSPDs [3,8–10].

Atomically layered two-dimensional (2D) semiconductors with low crystal symmetry have shown great potential in micro-nano PSPDs recently due to their intrinsically in-plane anisotropic properties [11,12]. For example, SnS, ReS_2, GeS_2, $GeAs_2$, AsP and black phosphorus (BP) exhibit an obvious in-plane anisotropy behavior in carrier transport, thermal conductivity, electrical conductivity, thermoelectric transport and optical absorption processes. They have potential application in PSPDs, polarization ultrafast lasers, polarization field effect transistors and polarization sensors [9–15]. Among them, BP-based PSPDs have the highest photocurrent anisotropy ratio of 0.59 [16], benefitting from its high carrier mobility and the strong in-plane anisotropy coming from the low-symmetry

puckered honeycomb crystal structure [17,18]. But with BP-based optoelectronic devices it is hard to get rid of the ambient degradation problem [19,20]. 2D layered indium selenide (InSe), which also has high carrier mobility and is more stable than BP in an atmospheric environment [21], exhibits huge potential for application in high-performance optoelectronic and electronic devices [22–27]. In addition, the anisotropic optical and electronic properties of 2D layered InSe have already been demonstrated in 2019 [28,29]. It is worth noting that InSe crystal has three specific polytypes, which are in β, γ and ε phases, respectively [30]. Among them, InSe in γ-phase and ε-phase belongs to the C_{3V}^5 and D_{3h}^1 symmetry groups respectively. Only the InSe in β-phase (β-InSe) belongs to the non-symmetry point group of D_{6h}^4, indicating that β-InSe exhibits better anisotropic optoelectronic properties than the other two polytypes.

In this work, p-type β-InSe single crystals are successfully prepared by controlling the composition via temperature gradient method. The morphology, structure and stability of the β-InSe flake are systematically investigated and characterized. The anisotropic nature of β-InSe has been unveiled by angle-resolved polarized Raman spectroscopy. Then experiments and theoretical calculations are carried out to explore the optical and electrical anisotropy of β-InSe. Finally, the polarization-sensitive photoresponse of photodetectors based on the β-InSe is demonstrated. The results reveal that a high photocurrent anisotropy ratio among single 2D-material-based PSPDs of 0.70 could be obtained from the β-InSe-based PSPDs, indicating its great potential in high-performance micro-nano PSPDs.

RESULTS

The single crystal of β-InSe in this work is grown via a temperature gradient method (see the Methods section), which has a hexagonal crystal structure stacked in AB order belonging to the non-symmetric D_{6h}^4 space group as shown in Fig. 1a. The morphology of the InSe samples is investigated by scanning electron microscopy (SEM) (Fig. 1b and c) and the cross section of the samples reveals the obvious layered structure of InSe. According to the results of the energy-dispersive x-ray spectroscopy (EDS), shown in Fig. S1 in the online supplementary file, the atomic ratio of indium to selenium is closed to 1 : 1 as designed, with a little excess of selenium. A photo of InSe bulk and the corresponding X-ray diffraction (XRD) pattern are shown in Fig. S2, where the diffraction peaks

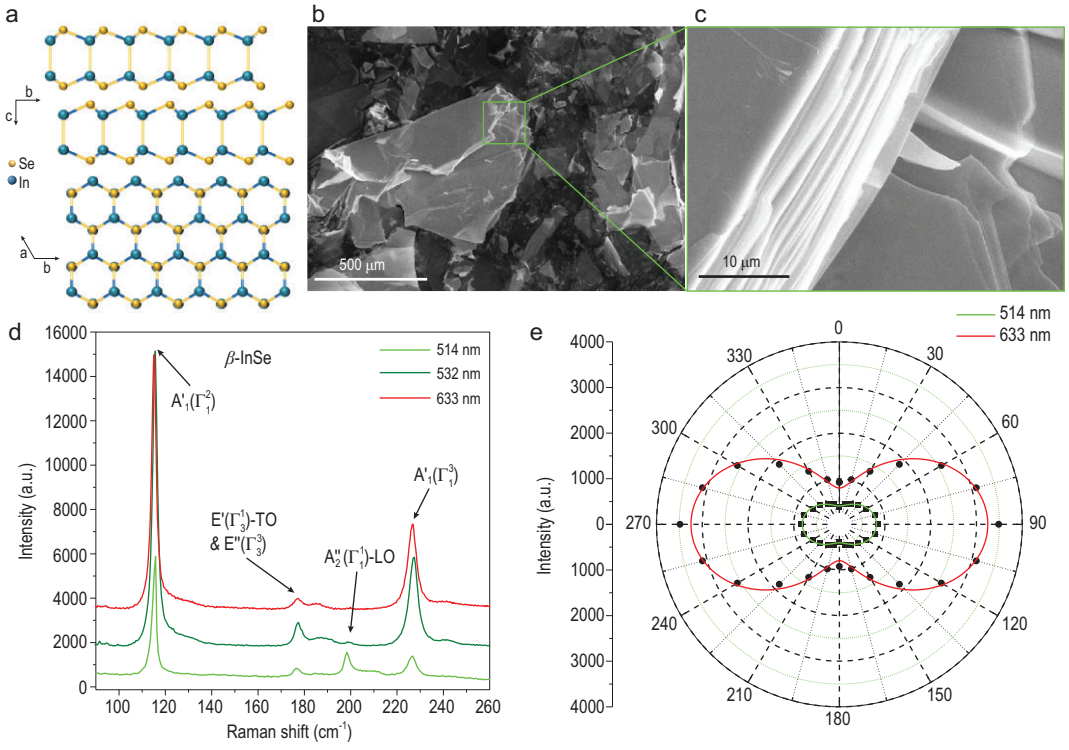

Figure 1. Structure and characterization of the few-layer β-InSe flake. (a) Front and top views of the hexagonal structure of the β-InSe crystal. (b and c) The SEM images of the same β-InSe flake with different magnification, revealing the layered structure of the β-InSe flake. (d) Raman spectra of β-InSe under 514, 532 and 633 nm laser excitations. (e) Polar plot of the angle-resolved polarized Raman intensity of $A_1'(\Gamma_1^3)$ vibrational modes of β-InSe under 514 and 633 nm excitations.

are in agreement with the standard crystal data of β-phase InSe (JCPDS No. 34-1431). The lattice parameters have been calculated to be a = 4.001 Å and c = 16.618 Å based on the XRD measurement. Figure 1d shows the unpolarized Raman spectra of the β-InSe flake on a silicon (Si) wafer, which has been calibrated by standard Si peak at 520.7 cm^{-1}. Three typical InSe Raman peaks at 115, 176 and 227 cm^{-1} corresponding to the out-of-plane $A_1^{'}(\Gamma_1^2)$, in-plane $E'(\Gamma_3^1) - TO$ & $E''(\Gamma_3^3)$ and out-of-plane $A_1^{'}(\Gamma_1^3)$ vibrational modes of InSe can all be observed under 514, 532 and 633 nm excitations. One resonance Raman peak at 199 cm^{-1} corresponding to the out-of-plane $A_2^{''}(\Gamma_1^1)$-LO vibrational mode can be observed under 514 nm (2.41 eV) excitation [31]. Figure 1e shows the polar plot of the angle-resolved polarized Raman intensity of the $A_1^{'}(\Gamma_1^3)$ vibrational mode. The intensity of $A_1^{'}(\Gamma_1^3)$ vibrational mode changes periodically with the polarization angle of the excitation, indicating a strong optical anisotropy of β-InSe. The same tendency of the polarized Raman spectra could be observed under resonance excitation (514 nm, Fig. S3) and non-resonance excitation (633 nm, Fig. S4). The angle-resolved polarized Raman spectra of β-InSe can be understood by the classical Raman selection rules and the crystal structure [10,32]. As shown in Fig. S5, when the thickness of the β-InSe sheet decreases, the anisotropic ratio of the $A_1^{'}(\Gamma_1^3)$ mode increases, which indicates that a thin layer possesses relatively high anisotropic Raman properties. The Raman spectroscopy of β-InSe has demonstrated a high in-plane optical anisotropy, indicating a great opportunity to exploit β-InSe-based PSPDs.

The back-gated structure of the β-InSe-based field effect transistor (FET) is shown in the inset of Fig. 2a. The thickness of the β-InSe flake is ~8 nm (Fig. S6), determined by atom force microscopy (AFM). The gate tunable output characteristics ($I_{ds} - V_{ds}$) (Fig. 2a) of the β-InSe-based FET show that the source-drain current I_{ds} increases at the same bias (V_{ds}) when gate voltage (V_g) varies from +60 V to −60 V. As shown in Fig. 2b, the transfer characteristics ($I_{ds} - V_g$) at V_{ds} = 1 V of the FET exhibit a p-type dominated ambipolar conduction behavior with an on/off current modulation of 10^5, which is one order larger than the requirement (10^4) for complementary metal oxide semiconductor (CMOS) logic devices [14]. The p-type conduction behavior is attributed to the existence of indium vacancies during the crystal growth. The atomic ratio of In to Se is ~44 : 56 according to the results of EDS spectra in Fig. S1b and the as-generated indium vacancies can serve as acceptor dopants [33,34]. The calculated field effect electron mobility is ~11.16 $cm^2 V^{-1} s^{-1}$ at room temperature in ambient air. This relatively low mobility might result from the scattering effect of air and SiO_2 substrate [14]. In addition, the β-InSe flakes and their FET exhibit good stability in air due to its specific ABAB stacking mode (as shown in Fig. S7), and there is almost no change on the morphology (Fig. S8) and Raman spectra (Fig. S9) of the β-InSe flake as well as the $I_{ds} - V_g$ curves of β-InSe FET (Fig. S10a) after being exposed in the air for 10 days. Besides, $I_{ds} - V_{ds}$ curves change little after being tested 13 times with a 1-minute interval (Fig. S10b), indicating a good operation stability.

For the photoresponse performance, as shown in Fig. 3a and b, I_{ds} and the photocurrent (I_{ph}) at V_g = 0 V of the β-InSe-based FET increase as the power intensity (P_{in}) of the laser beam is enlarged (λ = 800 nm) and reaches saturation when P_{in} is higher than 255.0 mW cm^{-2}. As the P_{in} dependent responsivity results show in Fig. 3c, the responsivity reaches the highest value of 194 A W^{-1} at the intensity of 2.2 mW cm^{-2} and 1 V bias. It is noteworthy that the responsivity is inversely proportional to the P_{in} of the laser beam, which results from the trap-related photogating effect reported previously [22,35,36]. The specific detectivity (D^*) reaches the highest value of 1.45 × 10^{12} Jones at the intensity of 2.2 mW cm^{-2} and 1 V bias. The deduction can be indirectly proven by the P_{in} dependence of I_{ph} at different bias in Fig. 3b, which satisfies the power law relation of $I_{ph} \propto P_{in}^{\alpha}$. The simulated index of power law α are ~0.26 (at V_{ds} = 1 V), ~0.26 (at V_{ds} = 2 V) and ~0.28 (at V_{ds} = 3 V), which are all much lower than 1, indicating a strong trap-related carrier recombination in the β-InSe-based FET [37]. For the dynamic photoresponse of the device, I_{ds} can be reproducibly switched from the 'on' state to the 'off' state with the rise time of ~620 μs and the decay time of ~540 μs, which indicates good

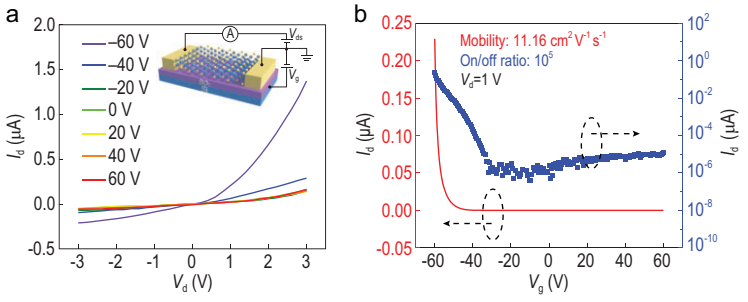

Figure 2. Electrical characterization of a few-layer β-InSe FET on a SiO_2/Si substrate. (a and b) Output transfer curves obtained from an 8-nm-thick device on a silicon substrate with 300 nm SiO_2 at room temperature and in the air. The inset of (a) is the schematic structure of a few-layer β-InSe FET. For the transfer curves in (b), the drain-source voltage is 1 V. The channel length and width of the device are 5 μm and 5 μm, respectively.

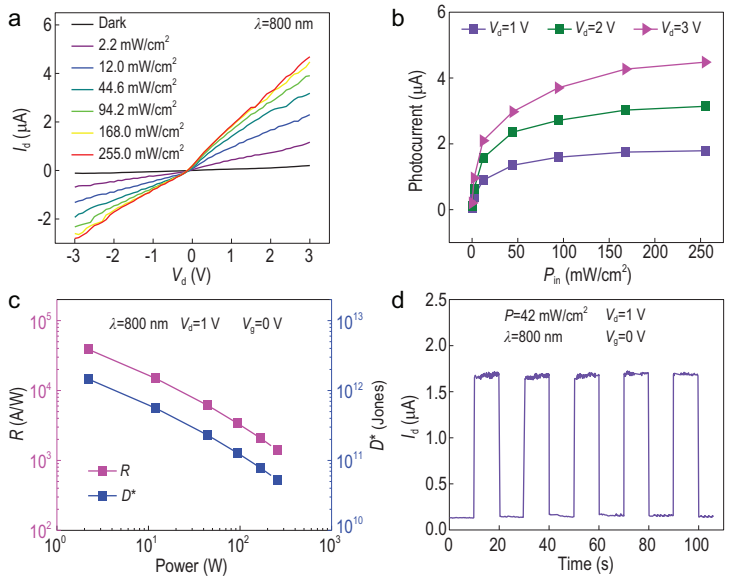

Figure 3. Photodetection performance of a few-layer β-InSe photodetector (L = 10 μm, W = 10 μm). (a) Output curves of a few-layer β-InSe photodetector in dark and under illumination with different excitation intensities at $\lambda = 800$ nm, $V_g = 0$ V. (b) Power-dependent photocurrent of the layer β-InSe photodetector at $V_{ds} = 1$ V, $V_{ds} = 2$ V and $V_{ds} = 3$ V, respectively. (c) Responsivity and specific detectivity as a function of illumination intensity at $\lambda = 800$ nm, $V_{ds} = 1$ V, $V_g = 0$ V. (d) A test of the photoswitching stability for the β-InSe device acquired at $\lambda = 800$ nm and P = 42 mW cm^{-2}, $V_{ds} = 1$ V, $V_g = 0$ V, showing that the rise time is ~22 ms and the decay time is ~24 ms.

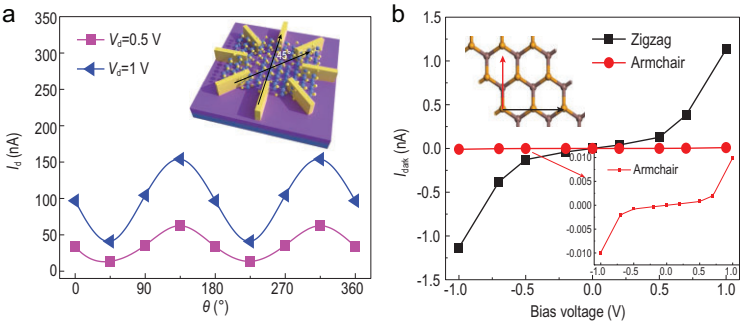

Figure 4. Anisotropic transport properties of few-layer β-InSe. (a) Angular dependence of the source-drain current of the device at $V_{ds} = 0.5$ V and $V_{ds} = 1$ V, respectively. The inset of (a) is the structure of the device for the angle-dependent transport behavior determination. (b) The DFT calculated dark current versus bias voltages along the zigzag and armchair directions. The top-left inset is the top view of the β-InSe structure, and the bottom-right inset is the dark current along the armchair direction.

reproducibility of the device, as shown in Fig. 3d and Fig. S11. The relatively slow response time may be improved by using graphene electrodes that have been proven in recent reports [38–44].

DISCUSSION

The β-InSe-based FET with eight electrodes (inset of Fig. 4a) has been fabricated to determine the angle-dependent transport behavior of β-InSe. The thickness of the β-InSe flake is measured to be 6.8 nm by AFM (Fig. S12). As shown in Fig. 4a, the angle-dependent dark current of device has the ratios of 4.62 ($V_{ds} = 0.5$ V) and 3.76 ($V_{ds} = 1$ V) for the maximum to minimum dark current at two orthogonal orientations. It suggests the obvious in-plane anisotropic conduction of β-InSe. Quantum transport calculation based on non-equilibrium Green's function density functional theory (NEGF-DFT) calculation has been carried out to determine the origin of the distinct anisotropic conduction behavior of β-InSe. As shown in Fig. S13, the supercell of the β-InSe hexagonal lattice has two perpendicular directions, armchair and zigzag. Due to the electrostatic potential profile difference between two directions, and the fact that the lattice energy-barrier scattering to Bloch waves along the armchair direction is more significant (Fig. S14), a large anisotropy of dark current can be predicted (Fig. 4b); the dark current along the zigzag direction might be theoretically two orders greater than that along the armchair direction.

Then the configuration in Fig. 5a is set up for testing the polarization sensitivity of β-InSe FET. As shown in Fig. 5b, the photocurrents dependent on the polarization angle demonstrate a shape of cosθ function in a period of π. In addition, the measured ratio of maximum to minimum photocurrent is ~5.66 at $V_{ds} = 1$ V. As a result, the photocurrent anisotropy ratio of our β-InSe devices is ~0.70 according to the formula $(I_{phmax} - I_{phmin})/(I_{phmax} + I_{phmin})$, which is ranking high among the single 2D-material-based PSPDs as shown in Table 1, except for one Te-nanosheet-based polarized infrared imaging system, which has an anisotropy ratio of 0.8 for 2.3 μm light [45]. The photocurrent changing with the polarized angle θ of incident light at 800 nm (1.55 eV) along the armchair direction has also been simulated by DFT. From the band structure of the β-InSe (Fig. S15), an indirect bandgap ~1.2 eV is observed. Figure 5c illustrates the orbital isosurface contributing to the photocurrent. Arrows indicate the light polarization angle θ, which is with respect to x axis along the armchair direction. The electron cloud isosurface shows that the main contribution is along the Se 4p_y direction. The transition possibility increases when the polarization direction parallels with the orbital dipoles. Hence, as shown in Fig. 5d, when $\theta = 0^\circ$ and 180°, light polarization is perpendicular to the Se 4p_y and the photocurrent reaches the minimum. When $\theta = 90^\circ$, light polarization is in line with Se 4p_y and the photocurrent reaches the maximum. A 0.67 anisotropic ratio of the photoresponse can be extracted from the theoretical calculation, which is a little smaller than the experimental

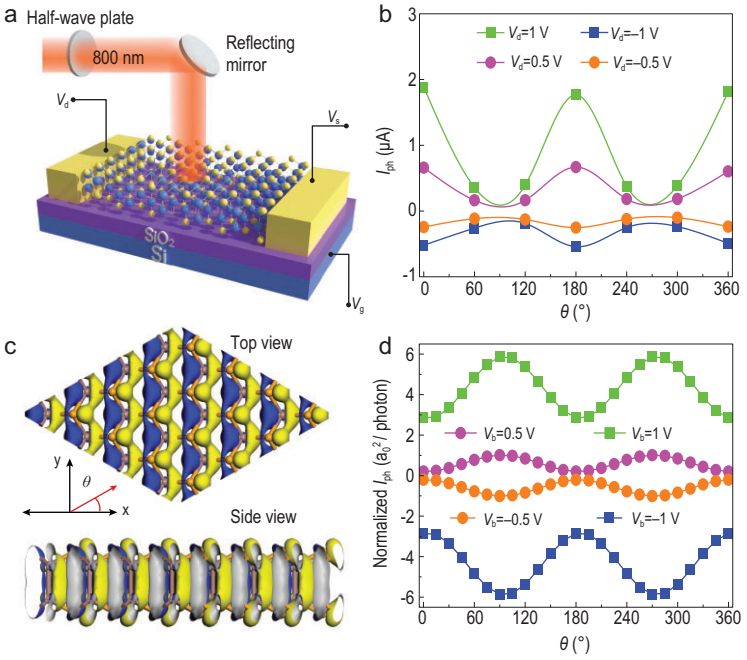

Figure 5. Polarization-sensitive photoresponse of the β-InSe FET. (a) The configuration for angle-dependent transport behavior determination. (b) Angular dependence of the photocurrent of the device at $V_{ds} = 0.5$ V and $V_{ds} = 1$ V, respectively. (c) Top view and side view of the contributing orbital to the photocurrent. Red arrow indicates the light polarization angle θ. (d) The quantum transport calculation of the photocurrent with different polarized angle θ for $\pm$0.5 V and $\pm$1.0 V bias voltages, when the light of the wavelength of 800 nm is irradiated.

Table 1. Anisotropic performance comparison of photodetectors made with different materials.

PSPDs	Bias (V)	Wavelength (nm)	Anisotropic ratio
ReS_2 [9]	1	532	0.54
SnS-$SnS_xSe_{(1-x)}$ [13]	7	532	0.082
$ReSe_2$ [14]	1	633	0.50
GeSe [3]	2	808	0.36
$GeAs_2$ [15]	1	532	0.33
GeS_2 [10]	10	325	0.35
GeSe/MoS_2 [1]	0	532	0.35
BP [16]	0.15	1550	0.59
Te [45]	1	2300	0.8
BP/InSe [8]	0	633	0.83
BP on WSe_2 [46]	0.5	1550	0.71
TiS_3/Si [47]	−0.5/0	660	0.29/0.44
Bi_2Te_3 [48]	1	635	0.23
Bi_2Te_3/CuPc [49]	0.01	650	0.44
InSe (this work)	1	800	0.70

one, 0.70. The reason for this smaller calculated one is that we did not take other electrons into account for the anisotropic photoresponse besides the Se $4p_y$. Both the experimental and theoretical results demonstrate a significant in-plane anisotropic photoresponse of β-InSe that is crucial for the realization of filter-free micro-nano PSPDs. As shown in Fig. S16, when the thickness of the β-InSe sheet decreases, the anisotropic ratio of the photoresponse performance will increase, which is in accordance with the layer-dependent anisotropic Raman result.

CONCLUSION

In summary, a p-type β-InSe single crystal is successfully prepared via temperature gradient method, which can be exfoliated into 2D layered flakes by tape-assisted mechanical exfoliation. The anisotropic nature of the β-InSe has been revealed by angle-resolved Raman. The out-of-plane vibrational modes exhibit pronounced periodic variations with the polarization angle of the excitations. Besides, a good stability of β-InSe flakes and their FET devices has been proven by AFM measurement and multi-repeat electrical performance test. The theoretical calculations are in good agreement with the experimental results in that there is strong anisotropic transport and a polarization-sensitive photoresponse in 2D layered β-InSe flakes. The photocurrent anisotropic ratio of the β-InSe photodetector reaches 0.70, which is ranking high among the single 2D-material-based PSPDs. The strong anisotropic Raman, transport and photoresponse properties of the β-InSe enable its great application potential in filter-free PSPDs.

METHODS

Preparation of β-InSe single crystal

A temperature gradient method has been used for β-InSe single crystal synthesis. A mixture of In and Se powders at a molar ratio 1 : 1 was placed in double-wall cleaned quartz ampoule down to a residual pressure of $\sim 10^{-4}$ Torr. The ampoules were kept in a vertical electrical furnace. Then the ampoules were slowly heated to 723 K at a rate of 20 K-1h to let indium and selenium react. After the reaction, the ampoules were heated to 1023 K at a rate of 10 K-1h and maintained at this temperature for 16 h to insure a complete reaction throughout the whole specimen. They were cooled down to 723 K slowly at a rate of 1 K-1h and finally cooled down at a rate of 20 K-1h to room temperature. The single crystal obtained was 25 mm in length and 13 mm in diameter. Increasing the soaking time to give enough time for a complete reaction between raw materials may be one way to improve the quality of the sample. And the rate of cool down of the furnace could be optimized, for example, 0.5 K-1h instead of 1 K-1h.

Device fabrication and measurement

Polarized Raman spectra have been obtained by a Jobin Yvon/HORIBA LabRam ARAMIS Raman spectrometer with 514, 633 and 785 nm lasers, where the polarization of the laser has been tuned by a Spectra-Physics automatic polarizer. The β-InSe FETs were fabricated according to the following steps. The few-layer β-InSe flakes were obtained by typical scotch tape assisted mechanical exfoliation of bulk β-InSe and transferred to a Si/SiO_2 (300 nm) wafer by using a polydimethylsiloxane (PDMS) thin film. Then methyl methacrylate (MMA) and polymethyl methacrylate (PMMA) have been spin-coated on the surface of the Si/SiO_2 wafer step-by-step. After that, electron-beam lithography (Raith Pioneer Two) and electron-beam evaporation were carried out to pattern the microscale Cr/Au (5 nm/50 nm) electrodes on β-InSe flakes. Following a lift-off process, β-InSe FETs were obtained. The β-InSe FETs were evaluated on a home-built probe station with a Keithley 4200 Semiconductor Parameter Analyzer, which is open to the air. The laser used for the photoconductivity measurements was generated from a coherent femtosecond laser.

Calculation method

We use a method based on NEGF-DFT to calculate the linear polarized photocurrent of β-InSe. β-InSe bulk structure belongs to $P63/_{mmc}$ space group. To calculate the photocurrent flow through β-InSe under linearly polarized light, we construct a two-probe device model for the armchair and zigzag directions. Generalized gradient approximation (GGA) expressed by the Perdew-Burke-Ernzerhof (PBE) is used to describe the exchange correlation functional. The maximum force acting on each atom becomes smaller than 0.03 eV/Å. The energy is optimized until it changes less than 10^{-5} eV/atom per step. The criteria for stress and displacement convergence are 0.05 GPa and 0.001 Å, respectively.

SUPPLEMENTARY DATA

Supplementary data are available at *NSR* online.

ACKNOWLEDGEMENTS

The authors acknowledge the equipment support from the Photonics Center of Shenzhen University for Micro/Nano-fabrication.

FUNDING

This work was supported by the National Key Research and Development Project (2019YFB2203503), the National Natural Science Foundation of China (61875138), the Natural Science Foundation of Guangdong Province for Distinguished Young Scholars (2018B030306038), the Innovation Team Project of Department of Education of Guangdong Province (2018KCXTD026), the Science and Technology Innovation Commission of Shenzhen (KQJSCX20180328095501798 and JCYJ20180507182047316) and the Scientific Research Fund of Jilin Provincial Education Department (JJKH20180550KJ).

AUTHOR CONTRIBUTIONS

Z.G., R.C. and H.W. conceived the idea and designed the experiments. R.C., H.W., Z.G., T.H.N., A.T.D. and X.C. performed the main synthesis, experimental measurements and data analysis. R.C., H.W., J.Z., F.M., B.Z. and P.-H.T. assisted with data analysis and interpretation. X.Z., D.K.S. and S.G. performed the theoretical simulation and calculation. Z.G., F.M. and H.Z. drafted the paper, and Y.Z., S.C. and D.F. provided revisions. All authors approved the final version of the paper for submission.

Conflict of interest statement. None declared.

REFERENCES

1. Xin Y, Wang X and Chen Z *et al.* Polarization-sensitive self-powered type-II GeSe/MoS_2 van der Waals heterojunction photodetector. *ACS Appl Mater Inter* 2020; **12**: 15406–13.
2. Tyo JS, Goldstein DL and Chenault DB *et al.* Review of passive imaging polarimetry for remote sensing applications. *Appl Optics* 2006; **45**: 5453–69.
3. Wang X, Li Y and Huang L *et al.* Short-wave near-infrared linear dichroism of two-dimensional germanium selenide. *J Am Chem Soc* 2017; **139**: 14976–82.
4. Gan MA, Shcheglov SA and Gan YM *et al.* Wide-angle optical systems with a combiner based on synthesized volume holograms for helmet-mounted displays. *J Opt Technol* 2008; **75**: 151–5.
5. Li L, Jin L and Zhou Y *et al.* Filterless polarization-sensitive 2D perovskite narrowband photodetectors. *Adv Opt Mater* 2019; **7**: 1900988.
6. Lim S, Ha M and Lee Y *et al.* Large-area, solution-processed, hierarchical $MAPbI_3$ nanoribbon arrays for self-powered flexible photodetectors. *Adv Opt Mater* 2018; **6**: 1800615.
7. Ma Z, Chai S and Feng Q *et al.* Chemical vapor deposition growth of high crystallinity Sb_2Se_3 nanowire with strong anisotropy for near-infrared photodetectors. *Small* 2019; **15**: 1805307.
8. Zhao S, Wu J and Jin K *et al.* Highly polarized and fast photoresponse of black phosphorus-InSe vertical p-n heterojunctions. *Adv Funct Mater* 2018; **28**: 1802011.
9. Liu F, Zheng S and He X *et al.* Highly sensitive detection of polarized light using anisotropic 2D ReS_2. *Adv Funct Mater* 2016; **26**: 1169–77.
10. Yang Y, Liu SC and Wang X *et al.* Polarization-sensitive ultraviolet photodetection of anisotropic 2D GeS_2. *Adv Funct Mater* 2019; **29**: 1900411.
11. Zhou Z, Cui Y and Tan PH *et al.* Optical and electrical properties of two-dimensional anisotropic materials. *J Semicond* 2019; **40**: 061001.

12. Yao J, Zheng Z and Yang G *et al.* Production of large-area 2D materials for high-performance photodetectors by pulsed-laser deposition. *Prog Mater Sci* 2019; **106**: 100573.
13. Xia J, Zhu D and Li X *et al.* Epitaxy of layered orthorhombic Sns-$SnS_xSe_{(1-x)}$ core–shell heterostructures with anisotropic photoresponse. *Adv Funct Mater* 2016; **26**: 4673–9.
14. Zhang E, Wang P and Li Z *et al.* Tunable ambipolar polarization-sensitive photodetectors based on high-anisotropy $ReSe_2$ nanosheets. *ACS Nano* 2016; **10**: 8067–77.
15. Li L, Gong P and Sheng D *et al.* Highly in-plane anisotropic 2D $GeAs_2$ for polarization-sensitive photodetection. *Adv Mater* 2018; **30**: 1804541.
16. Long M, Gao A and Wang P *et al.* Room temperature high-detectivity mid-infrared photodetectors based on black arsenic phosphorus. *Sci Adv* 2017; **3**: e1700589.
17. Xia F, Wang H and Jia Y *et al.* Rediscovering black phosphorus as an anisotropic layered material for optoelectronics and electronics. *Nat Commun* 2014; **5**: 4458.
18. Qiao J, Kong X and Hu ZX *et al.* High-mobility transport anisotropy and linear dichroism in few-layer black phosphorus. *Nat Commun* 2014; **5**: 4475.
19. Zhou Q, Chen Q and Tong Y *et al.* Light-induced ambient degradation of few-layer black phosphorus: mechanism and protection. *Angew Chem Int Ed* 2016; **55**: 11437–41.
20. Kim M, Kim HG and Park S *et al.* Intrinsic correlation between electronic structure and degradation: from few-layer to bulk black phosphorus. *Angew Chem Int Ed* 2019; **58**: 3754–8.
21. Politano A, Chiarello G and Samnakay R *et al.* The influence of chemical reactivity of surface defects on ambient-stable InSe-based nanodevices. *Nanoscale* 2016; **8**: 8474–9.
22. Tamalampudi S, Lu YY and Kumar UR *et al.* High performance and bendable few-layered InSe photodetectors with broad spectral response. *Nano Lett* 2014; **14**: 2800–6.
23. Bandurin DA, Tyurnina AV and Yu GL *et al.* High electron mobility, quantum Hall effect and anomalous optical response in atomically thin InSe. *Nat Nanotechnol* 2017; **12**: 223–7.
24. Arora H and Erbe A. Recent progress in contact, mobility, and encapsulation engineering of InSe and GaSe. *Infomat* 2021; **3**: 662–93.
25. Boukhvalov DW, Gurbulak B and Duman S *et al.* The advent of Indium Selenide: synthesis, electronic properties, ambient stability and applications. *Nanomaterials* 2020; **7**: 372.
26. Liu L, Wu L and Wang A *et al.* Ferroelectric-gated InSe photodetectors with high on/off ratios and photoresponsivity. *Nano Lett* 2020; **20**: 6666–73.
27. Jang H, Seok Y and Choi Y *et al.* High-performance near-infrared photodetectors based on surface-doped InSe. *Adv Funct Mater* 2021; **31**: 2006788.
28. Hamer MJ, Zultak J and Tyurnina AV *et al.* Indirect to direct gap crossover in two-dimensional InSe revealed by angle-resolved photoemission spectroscopy. *ACS Nano* 2019; **13**: 2136–42.
29. Shubina TV, Desrat W and Moret M *et al.* InSe as a case between 3D and 2D layered crystals for excitons. *Nat Commun* 2019; **10**: 3479.
30. Yang Z, Jie W and Mak CH *et al.* Wafer-scale synthesis of high-quality semiconducting two-dimensional layered InSe with broadband photoresponse. *ACS Nano* 2017; **11**: 4225–36.
31. Lei S, Ge L and Najmaei S *et al.* Evolution of the electronic band structure and efficient photo-detection in atomic layers of InSe. *ACS Nano* 2014; **8**: 1263–72.
32. Wu J, Mao N and Xie L *et al.* Identifying the crystalline orientation of black phosphorus using angle-resolved polarized Raman spectroscopy. *Angew Chem Int Ed* 2015; **54**: 2366–9.
33. Xiao K, Carvalho A and Neto AH *et al.* Defects and oxidation resilience in InSe. *Phys Rev B* 2017; **96**: 054112.
34. Zhao Q, Wang W and Carrascoso-Plana F *et al.* The role of traps in the photocurrent generation mechanism in thin InSe photodetectors. *Mater Horiz* 2020; **7**: 252–62.
35. Island JO, Blanter SI and Buscema M *et al.* Gate controlled photocurrent generation mechanisms in high-gain In_2Se_3 phototransistors. *Nano Lett* 2015; **15**: 7853–8.
36. Fang H and Hu W. Photogating in low dimensional photodetectors. *Adv Sci* 2017; **4**: 1700323.
37. Mihailetchi VD, Xie H and de Boer B *et al.* Charge transport and photocurrent generation in poly(3-hexylthiophene): methanofullerene bulk-heterojunction solar cells. *Adv Funct Mater* 2006; **16**: 699–708.
38. Wei X, Yan F and Lv Q *et al.* Enhanced photoresponse in $MoTe_2$ photodetectors with asymmetric graphene contacts. *Adv Opt Mater* 2019; **7**: 1900190.
39. Massicotte M, Schmidt P and Vialla F *et al.* Picosecond photoresponse in van der Waals heterostructures. *Nat Nanotechnol* 2016; **11**: 42–7.
40. Wei X, Yan F and Lv Q *et al.* Fast gate-tunable photodetection in the graphene sandwiched WSe_2/GaSe heterojunctions. *Nanoscale* 2017; **9**: 8388–92.
41. Zhang K, Fang X and Wang Y *et al.* Ultrasensitive near-infrared photodetectors based on a graphene-$MoTe_2$-graphene vertical van der Waals heterostructure. *ACS Appl Mater Interfaces* 2017; **9**: 5392–8.
42. Lv Q, Yan F and Wei X *et al.* High-performance, self-driven photodetector based on graphene sandwiched GaSe/WS_2 heterojunction. *Adv Opt Mater* 2018; **6**: 1700490.
43. Lee CH, Lee GH and van der Zande A *et al.* Atomically thin p–n junctions with van der Waals heterointerfaces. *Nat Nanotechnol* 2014; **9**: 676–81.
44. Luo W, Cao Y and Hu P *et al.* Gate tuning of high-performance InSe-based photodetectors using graphene electrodes. *Adv Opt Mater* 2015; **3**: 1418–23.
45. Tong L, Huang X and Wang P *et al.* Stable mid-infrared polarization imaging based on quasi-2D tellurium at room temperature. *Nat Commun* 2020; **11**: 2308.
46. Ye L, Wang P and Luo W *et al.* Highly polarization sensitive infrared photodetector based on black phosphorus-on-WSe_2 photogate vertical heterostructure. *Nano Energy* 2017; **37**: 53–60.
47. Niu Y, Frisenda R and Flores E *et al.* Polarization-sensitive and broadband photodetection based on a mixed-dimensionality TiS_3/Si p-n junction. *Adv Opt Mater* 2018; **6**: 1800351.
48. Yao J, Shao J and Li S *et al.* Polarization dependent photocurrent in the Bi_2Te_3 topological insulator film for multifunctional photodetection. *Sci Rep* 2015; **5**: 14184.
49. Yang M, Wang J and Zhao Y *et al.* Polarimetric three-dimensional topological insulators/organics thin film heterojunction photodetectors. *ACS Nano* 2019; **13**: 10810–7.

Supplementary Information for *National Science Review*

High performance polarization sensitive photodetectors on two dimensional β-InSe

Zhinan Guo[1], Rui Cao[1], Huide Wang[1], Xi Zhang[2], Fanxu Meng[1], Xue Chen[5], Siyan Gao[2], David K. Sang[1], Thi Huong Nguyen[3], Anh Tuan Duong[3], Jinlai Zhao[1], Yu-Jia Zeng[1], Sunglae Cho[3], Bing Zhao[4], Ping-Heng Tan[5], Han Zhang[1,*], and Dianyuan Fan[1]

[1] Institute of Microscale Optoelectronics, International Collaborative Laboratory of 2D Materials for Optoelectronics Science and Technology, College of Physics and Optoelectronic Engineering, Shenzhen University, Shenzhen, 518060, P. R. China.

[2] Institute of Nanosurface Science and Engineering, Guangdong Provincial Key Laboratory of Micro/Nano Optomechatronics Engineering, Shenzhen University, Shenzhen 518060, P. R. China.

[3] Department of Physics and Energy Harvest-Storage Research Center, University of Ulsan, Ulsan 680-749, Republic of Korea.

[4] State Key Laboratory of Supramolecular Structure and Materials, Jilin University, Changchun 130012, China.

[5] State Key Laboratory of Superlattices and Microstructures, Institute of Semiconductors, Chinese Academy of Sciences, Beijing 100083, China.

* Correspondence and requests for materials should be addressed to Han Zhang (email: hzhang@szu.edu.cn).

Zhinan Guo, Rui Cao, Huide Wang, and Xi Zhang contribute equally to this work.

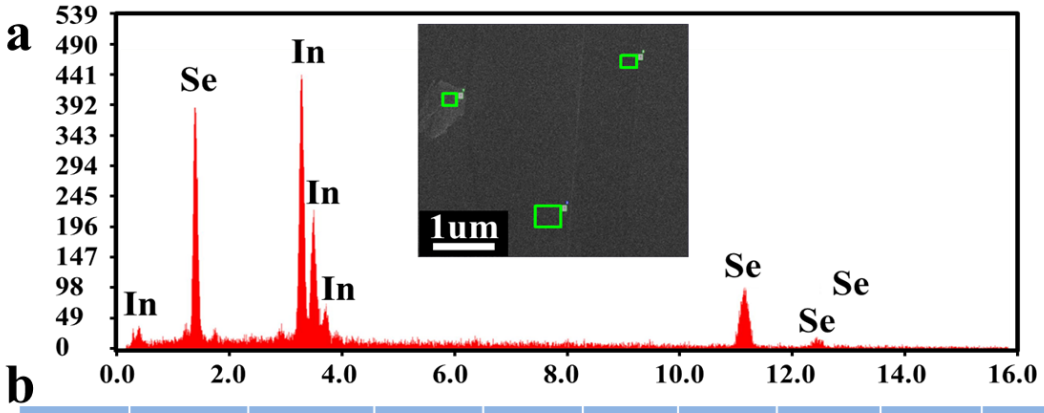

Element	Weight%	Atomic%	Net Int.	Error%	Kratio	Z	R	A	F
InL	53.39	44.07	109.18	5.32	0.463	0.988	1.045	0.863	1.019
SeK	46.61	55.93	43.89	6.97	0.528	1.026	0.969	0.970	1.137

Figure S1. EDS test of the *β*-InSe sheet. (a) EDS spectra and (b) data of the *β*-InSe sheet for the scanned area of the green box in the inset, showing the atomic ratio of In atomic and Se atomic of the *β*-InSe sheet is almost 1:1.

Inductively coupled plasma atomic emission spectroscopy (ICP-AES, Agilent 7700x) has used to obtain a more accurate atomic ratio of In to Se. The mass percentage results of the dissolved *β*-InSe sample output by the ICP-AES measurement are In 560.839 ppb for In and 410.602 ppb for Se, which means the real atomic ratio of In to Se is 48.35:51.65.

a

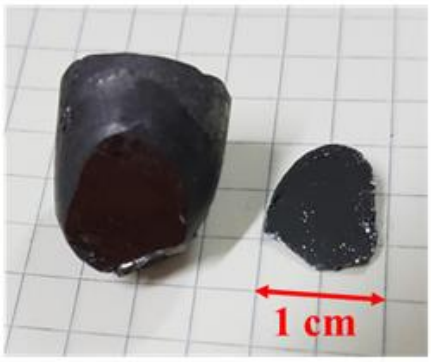

b

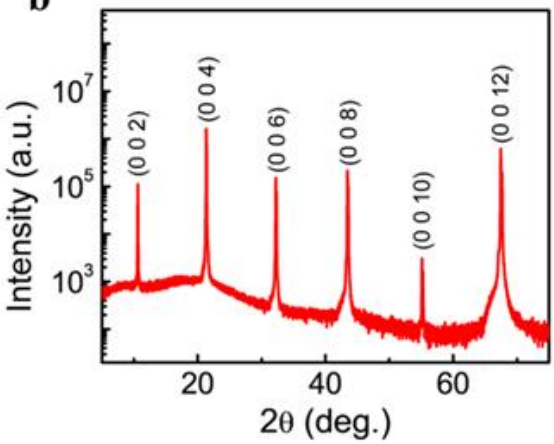

c

	a(Å)	c(Å)
JPCD 34-1431	4.005	16.640
InSe_powder	4.001	16.618

Figure S2. (a) Photo and (b,c) XRD result of InSe sample, which demonstrate the material is β-InSe.

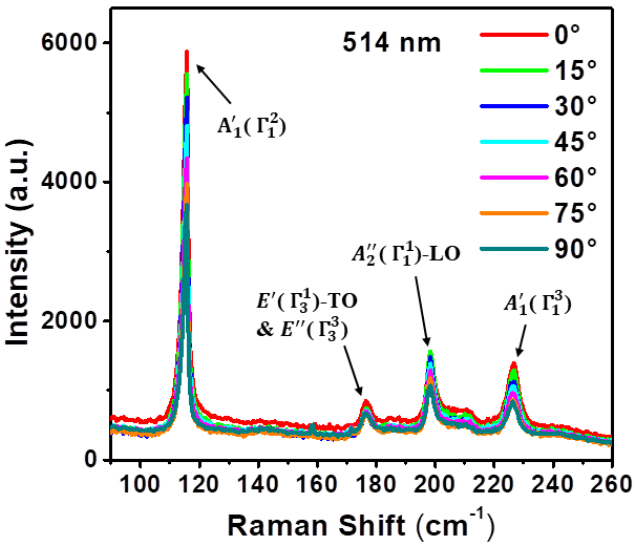

Figure S3. Polarized Raman spectra of the β-InSe sheet with different polarization angle under 514 nm excitation.

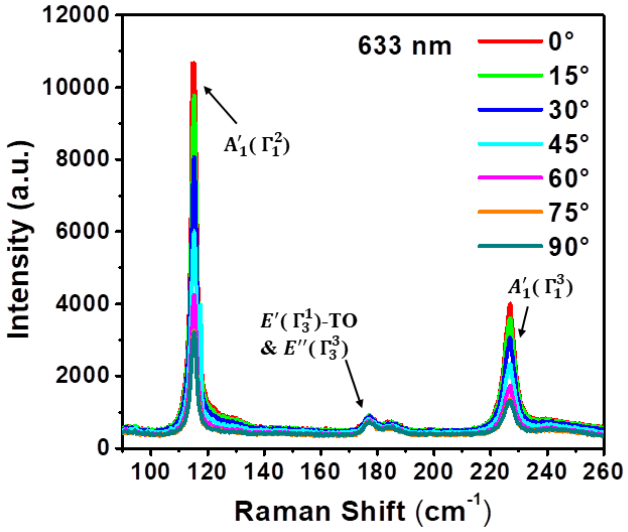

Figure S4. Polarized Raman spectra of the β-InSe sheet with different polarization angle under 633 nm excitation.

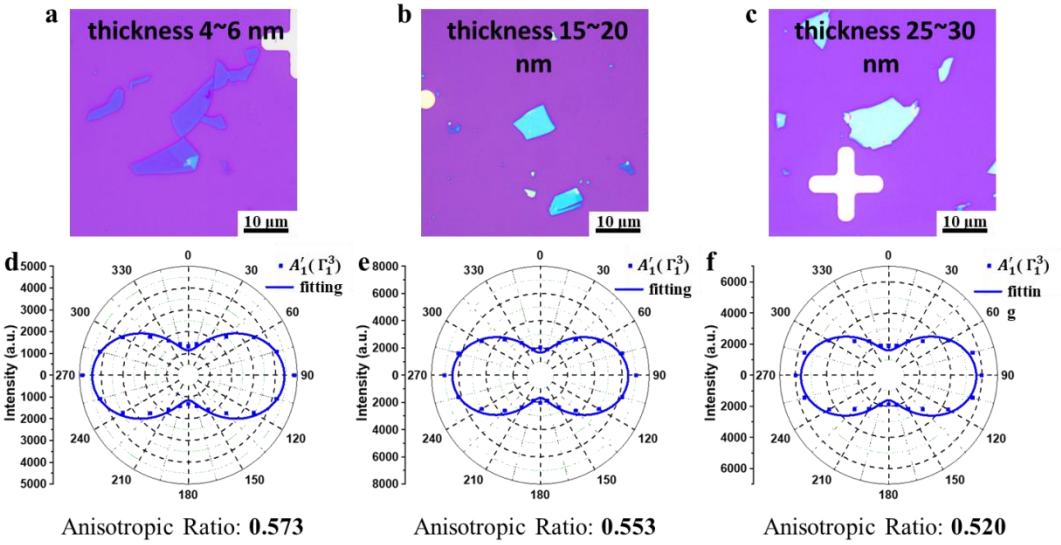

Figure S5. Optical images and thickness-dependent polarization-Raman spectra of three *β*-InSe nanosheets with different thickness: thin one (a, d), middle one (b, e), and thick one (c, f).

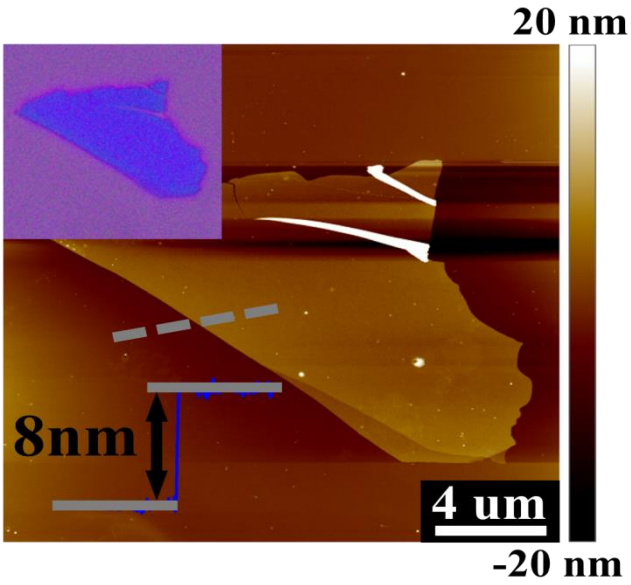

Figure S6. The optical (inset) and AFM images of the few-layer β-InSe sheet for FET fabrication.

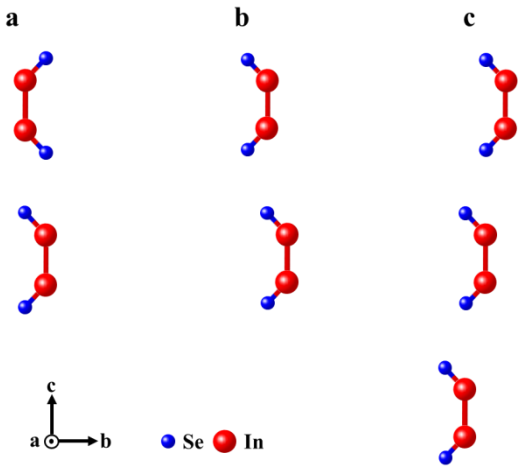

Figure S7. Unit cell of InSe phases: (a) β-InSe, (b) ε-InSe and (c) γ-InSe.

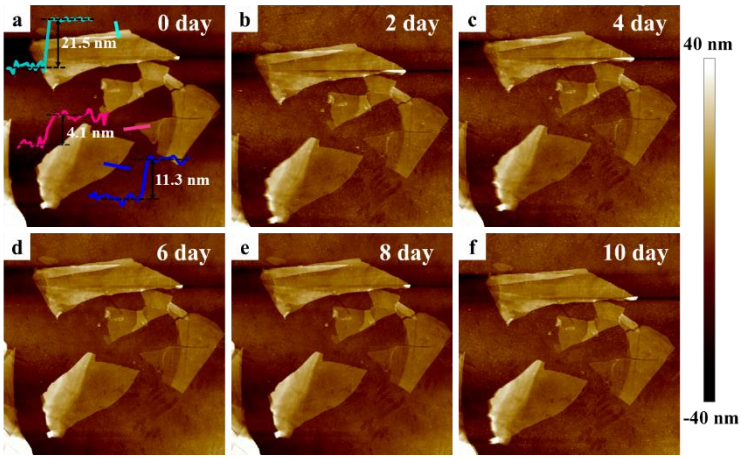

Figure S8. Morphology of few-layer β-InSe sheets at different time in the air. AFM images of a few-layer β-InSe sheet (~ 4.1 nm, ~ 11.3 nm, and ~ 21.5 nm) exposed to air for (a) 0 day, (b) 2 days, (c) 4 days, (d) 6 days, (e) 8 days (f) 10 days, revealling the robust stability of the few-layer β-InSe sheet with different thickness.

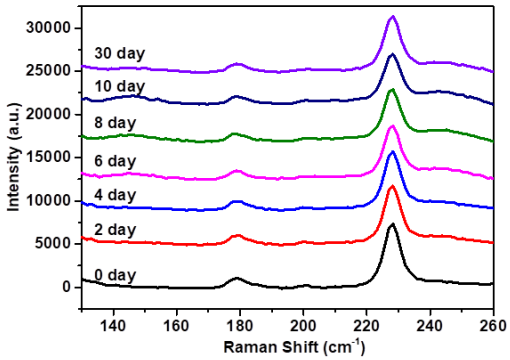

Figure S9. Raman spectra of few-layer β-InSe sheet at different time in the air.

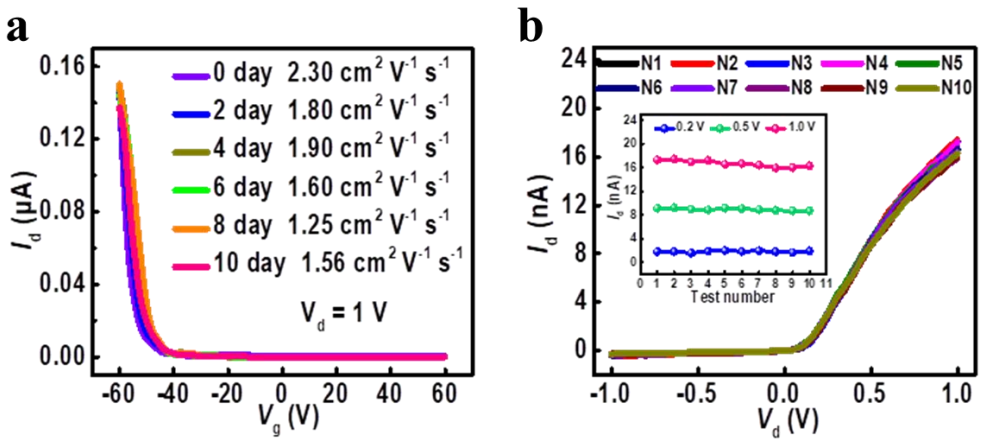

Figure S10. Stability of electrical characterization of a few-layer *β*-InSe FET. (a) Current to gate voltage curve obtained from a *β*-InSe FET device after air exposure for 0-10 day for comparison at V_{ds} = 1 V. (b) Current to drain-source voltage curve obtained from a *β*-InSe FET device at thirteen times with 1-minute interval. Inset: Current to test number curve at V_{ds} = 1 V, V_{ds} = 2 V and V_{ds} = 3 V, respectively.

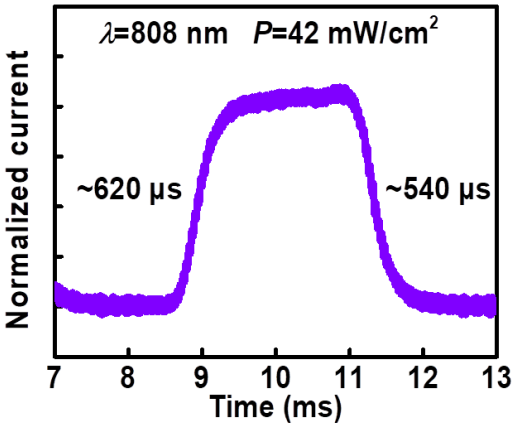

Figure S11. Response time of the device under 808 nm light illumination during one cycle.

The calculation process of the performance parameters of the photodetector

The responsivity (R) can be calculated by the formula:

$R = I_{ph} / (P_{in} A)$

where I_{ph} is the photocurrent, P_{in} is the laser power density, A is area of the photodetector channel.

The specific detectivity (D^*) can be calculated by the approximate calculation formula:

$D^* = R A^{1/2} / (2e I_{dark})^{1/2}$

where e is the electron charge, and I_{dark} is the dark current [1].

Reference

[1] Wu F. *et al*. AsP/InSe Van der Waals Tunneling Heterojunctions with Ultrahigh Reverse Rectification Ratio and High Photosensitivity. *Adv Funct Mater* 2019; **29**: 1900314.

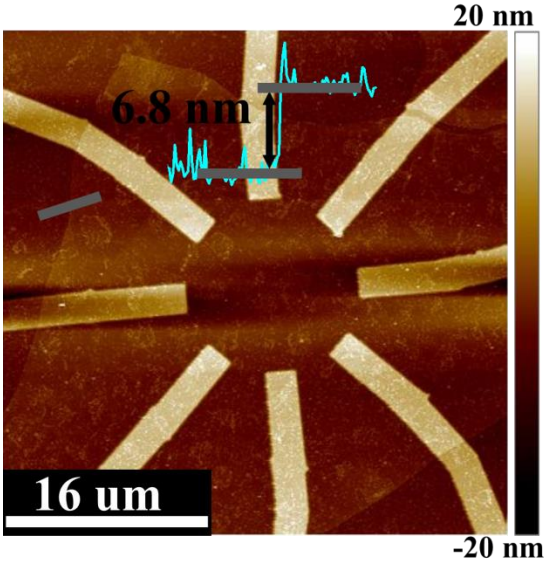

Figure S12. Morphology of the β-InSe based device for determining the angle-dependent transport behavior and the thickness of β-InSe flake is ~6.8 nm according to the profile.

Principle investigation of strong anisotropy of photo-response in *β*-InSe via density functional theory

(1) Construction of structure

β-InSe bulk structure belongs to P63/$_{mmc}$ space group. The optimized bulk *β*-InSe has lattice constants *a1* = *a2* = 4.113 Å. As shown in the Figure 1aa, the supercell of *β*-InSe hexagonal lattice has two perpendicular directions, armchair and zigzag. To calculate the photocurrent flow through *β*-InSe under linearly polarized light, we construct a two-probe device model for the armchair and zigzag directions. As shown in the Figure S5, the top and side views of the *β*-InSe photodetector in the armchair and zigzag direction.

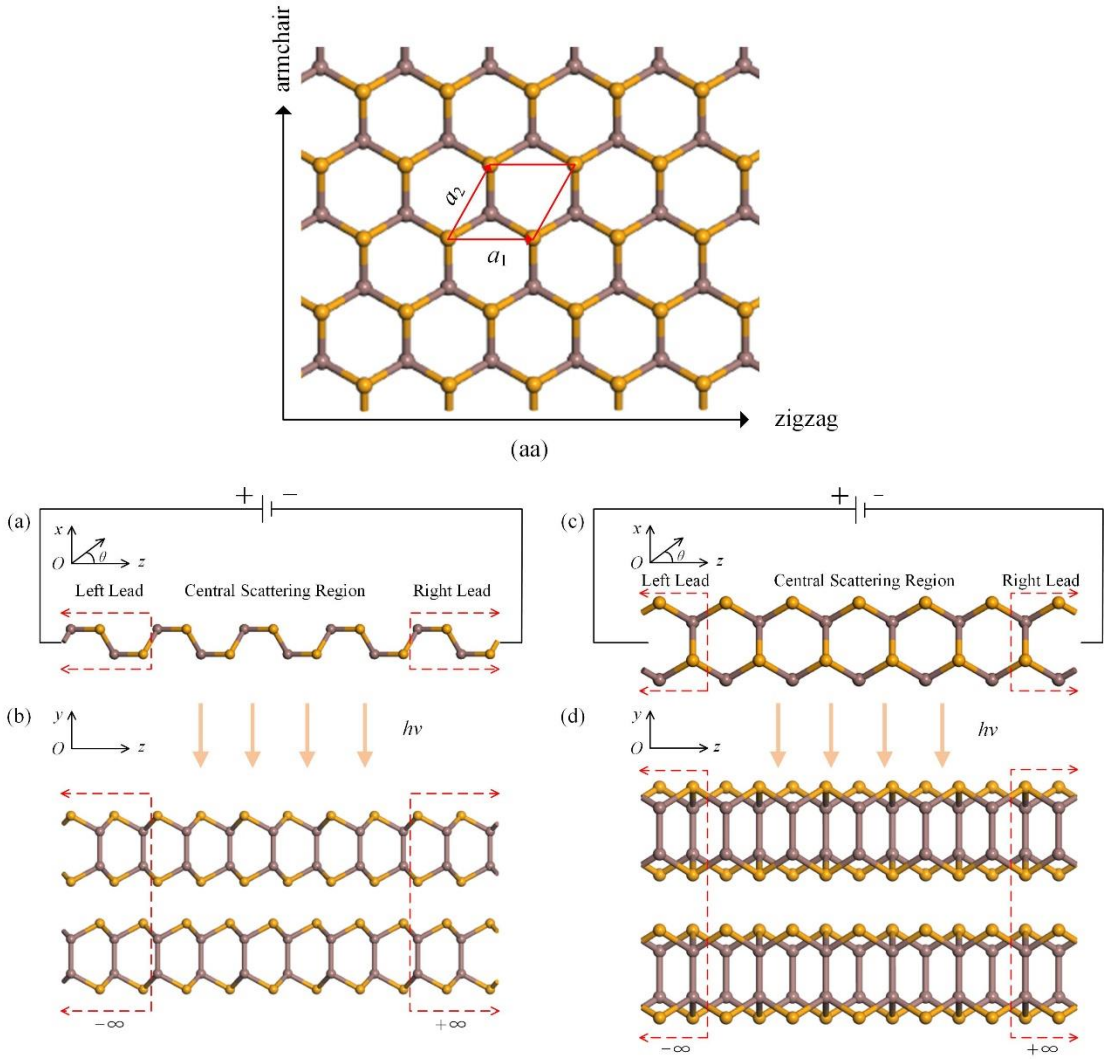

Figure S13. Construction of the β-InSe crystal structure. (aa) Top-view of β-InSe supercell. a_1 and a_2 denotes the basis vectors of the hexagonal lattice. Arrows indicate the armchair and zigzag directions. (a) Top-view and (b) side-view two-probe device along armchair direction. (c) Top-view and (d) side-view two-probe device along zigzag direction. The angle θ denotes the polarization angle of linear light with respect to the current direction. The red dashed lines represent the left and right lead, respectively. The remaining is the scattering region. The arrows indicate the polarized light used to irradiate the entire scattering region.

The two-probe device consists of three parts: a scattering region, the left and right lead structures, which extend to $\pm\infty$ along the transport direction, respectively. The current direction is set along the armchair direction in (a)-(b) and zigzag direction in (c) and (d) of the β-InSe. Bias was applied on the left lead against the right lead. The central section is where the photocurrent flows from the left lead to right lead acrossing the scattering region. The whole scattering region is irradiated perpendicularly with linearly polarized light. The polarization direction forms an angle θ with respect to the current direction.

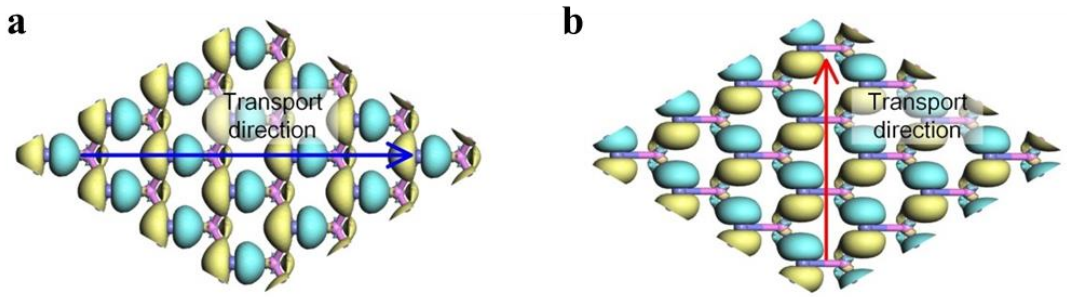

Figure S14. The calculated Bloch waves of Se orbitals. (a) Bloch waves of Se 4*px* orbital along the armchair direction; (b) Bloch waves of Se 4*py* orbital along the zigzag direction.

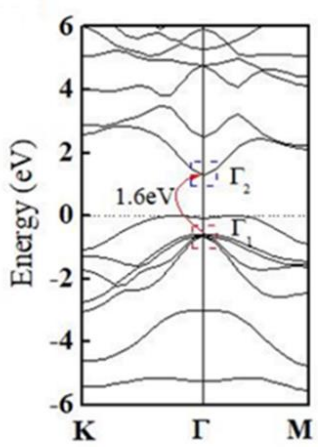

Figure S15. The band structure of β-InSe.

From the band structure of the β-InSe, an indirect bandgap about 1.2 eV is observed. The valence band maximum (VBM) occurs between the K point and Γ point, while the conduction band minimum (CBM) is located at the Γ point. Fig. S15 shows the composition of the transition molecular orbitals of Γ_1 and Γ_2 which are two superposition orbitals mainly denoted by Se $4p_y$ and $4p_x$ atomic orbitals.

(2) Computational details

Here, structural optimization is performed using the Nanodcal. Generalized gradient approximation (GGA) expressed by the Perdew-Burke-Ernzerhof (PBE) is used to describe the exchange correlation functional. The maximum force acting on each atom becomes smaller than 0.03 eV/Å. The energy is optimized until it changes less than 10^{-5} eV/atom. The criterion for stress and displacement convergence are 0.05 GPa and 0.001 Å, respectively. In addition, the double-ξ plus polarization (DZP) basis set is employed in this calculation. To avoid the interaction between slabs in the neighboring unit cells, a vacuum space along the z direction is set to 20 Å.

(3) Photocurrent calculations

In this work, we use a method based on density functional theory within Keldysh nonequilibrium Green's function (NEGF-DFT) to calculate the photocurrent. Specifically, the electron-photon interaction is treated as a perturbation on the self-consistent Hamiltonian of the system (H_0). Therefore, the total Hamiltonian of the

electron-photon system can be written as:

$$\hat{H} = \hat{H}_0 + \frac{e}{m_0}\mathbf{A}\cdot\hat{\mathbf{p}}$$

Where **A** is the polarization vector of the light. The Green's functions are written as :

$$G^{<} = G^{0r}(i\Gamma_L f_L + i\Gamma_R f_R + \sum\nolimits_{ph}^{<})G^{0a}$$

$$G^{>} = G^{0r}(i\Gamma_L(1-f_L) + i\Gamma_R(1-f_R) + \sum\nolimits_{ph}^{>})G^{0a}$$

Where Γ is the linewidth function of the electrodes, represents the coupling of the device scattering region to the electrodes. G^{0r} is the retarded Green's functions without photon. G^{0a} is the advanced Green's functions without photon. The photoinduced current is calculated by as follow:

$$I_{ph} = \frac{e}{2\hbar}\int\frac{dE}{2\pi}\sum_{\alpha}T_{\alpha}(E)$$

Where α represent the lead of source/drain. $T_\alpha(E)$ is the effective transmission coefficient of lead α, which can be expressed as:

$$T_{\alpha}(E) = Tr\left\{i\Gamma_{\alpha}[(1-f_{\alpha})G_{ph}^{<} + f_{\alpha}G_{ph}^{>}]\right\}$$

Where Γ_α represents the line-width function which describes the interactions between the lead α and the scattering regions. f_α is the Fermi distribution function of lead α. $G_{ph}{}^{<}$ and $G_{ph}{}^{>}$ denote the zeroth order approximations of the smaller and greater Green's functions based on the Keldysh equation. From above, we calculate the normalized photocurrent, the photoresponse function can be written as :

$$R = \frac{I_{ph}}{eI_{\omega}}$$

Where I_ω is the photon flux.

Thickness dependent anisotropy photoresponse of the *β*-InSe photodetector

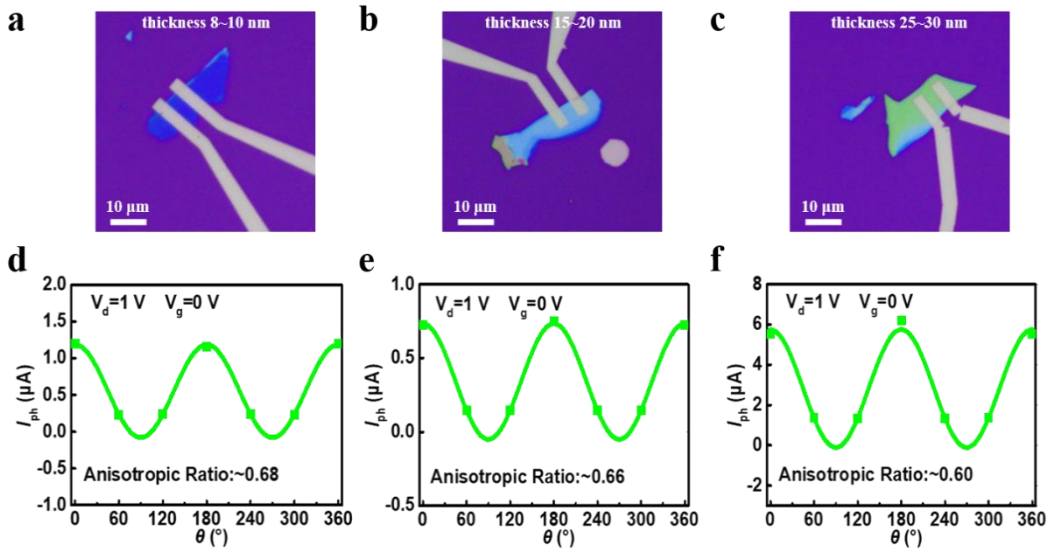

Figure S16. Optical images and thickness-dependent anisotropy photoresponse of the *β*-InSe photodetectors: thin one (a, d), middle one (b, e), and thick one (c, f).